Modeling Galactic Gas Disk Settling

Eric I. Barnes [1], Joel E. Tohline, Juhan Frank
Department of Physics & Astronomy, Louisiana State University, Baton Rouge, LA 70802
barnesy@physics.rutgers.edu
tohline@physics.lsu.edu
frank@physics.lsu.edu
and

Paul L. Fisher
Department of Physics, University of Louisiana Monroe, Monroe, LA 71209
phfisher@ulm.edu

ABSTRACT

The mechanism underlying the origin and maintenance of the warps observed in the neutral hydrogen disks of spiral galaxies is undetermined. One possible explanation of this phenomenon is investigated here by following the evolutions of nonself-gravitating gaseous disks that are initially inclined to the equatorial plane of a spheroidal, logarithmic potential. Disks in three separate oblate potentials behave in similar manners. The evolutions of these disks mimic nonself-gravitating particle disks at early times. As differential precession proceeds and the disks warp, pressure effects become important and the disks eventually settle to the potentials' equatorial planes while retaining some nonaxisymmetric character.

1. Introduction–REALLY Rough draft version

1.1. Observations of Warps

The 21-cm emission from neutral hydrogen has been used to map HI distributions in disk galaxies for several decades. These gas disks very often appear to be corrugated, lopsided, and to have central holes, regions with very little or no emission (e.g., Giovanelli & Haynes 1988, Chaves & Irwin 2001). These holes give the disks the appearance of tori. It was also quickly recognized that the HI disks of many spiral galaxies (including the Milky Way) show clear evidence of nonaxisymmetric warped features (Lewis 1968; Gordon 1971; Wright, Warner, & Baldwin 1972; Sancisi 1976; Bosma 1981). When seen edge-on, warped HI disks appear integral-sign shaped, with the gas at large radii extending above the flat central disk on one side and below on the opposite side. However, it is not necessary to observe an edge-on galaxy to discern the presence of a warp. Rogstad, Lockhart, & Wright (1974) showed that the observed velocity fields of spiral galaxies at arbitrary inclinations can betray the presence of warps. These warped disks can be modeled as systems of rigid, concentric annuli which can have independent orientations. The annuli can be tilted with respect to the plane describing the flat inner disk. The points at which the annuli cross this plane lie on the line of nodes. If the annuli are simply tilted with respect to one another, the line of nodes will be a straight line perpendicular to the warp direction. In more complex situations, another angle is needed to specify the annuli orientations. This is the twist angle, and it describes how the line of nodes changes with radius. More recently, Briggs (1990) has summarized his observations of warps in four rules, two of which we paraphrase here. One, warps generally become evident between the de Vaucouleurs radius (R_{dV}, surface brightness at

[1] Currently at Department of Physics & Astronomy, Rutgers University, Piscataway, NJ 08854

$R_{dV} = 25\,\mu_{\rm B}$) and the Holmberg radius (R_H, surface brightness at $R_H = 26.5\,\mu_{\rm photographic}$), i.e., outside the optical radius. Two, inside R_H the line of nodes is straight, while outside R_H the line of nodes generally has a leading spiral shape.

1.2. Theories of Warps

There have been numerous theoretical studies of warped disk structures in galaxies. The warp that is present in the Milky Way was first hypothesized to be due to its motion relative to Local Group intergalactic matter (Kahn & Woltjer 1959). Alternatively, Hunter & Toomre (1969) modeled the Milky Way warp as the result of a tidal encounter with the Large Magellanic Cloud. Tidal interactions are convenient instigators of warps, but isolated galaxies, such as NGC 5907 (Sancisi 1976), also have warps. Binney (1978, 1981) investigated vertical instabilities of orbits as a method of producing warps. A possible connection between magnetic fields and warps has also been discussed (e.g., Battaner, Florido, & Sanchez-Saavedra 1990, Fletcher & Shukurov 2001). Recently, López-Corredoira, Betancort-Rijo, & Beckman (2002) have proposed a variant of the Kahn & Woltjer (1959) idea that intergalactic material causes warps. In their proposal, the accretion of material onto the galactic disk brings about an angular momentum transfer which effectively torques the disk.

Lynden-Bell (1965) first discussed the idea that misalignment of disk angular momentum and the symmetry axis of the underlying gravitational potential could be the root cause of warps. The interested reader is pointed to van den Bosch *et al.* (2002) for a discussion of this phenomenon in recent cosmological N-body/SPH simulations. The possibility that warps generated in such a manner could exist for many galactic rotation periods was discussed by Tubbs & Sanders (1979). This idea was also used in attempts to discern the geometric structure of elliptical galaxies containing gas/dust disks (Tubbs 1980; Tohline, Simonson, & Caldwell 1982). Further studies based on the misalignment hypothesis have varied between numerical studies of self-gravitating particle systems in various galactic potentials (Sparke 1986; Sparke & Casertano 1988; Hofner & Sparke 1994) and analytical investigations of viscous, nonself-gravitating systems (Steiman-Cameron & Durisen 1988, 1990; New *et al.* 1998). This paper focuses on fully three-dimensional hydrodynamic simulations of nonself-gravitating gaseous disk settling in an external potential. We begin by detailing the framework of our simulations in §2. The results of several particle simulations are presented in §3. Section 4 contains discussions of the initial conditions, the hydrodynamics code, and the results of the evolutions. An analysis of the gas settling simulations is given in §5. Finally, the conclusions of this study are presented in §6.

2. Potentials & Coordinate Systems

We have investigated the settling behavior of a gas disk in three separate oblate spheroidal potentials. Specifically, the initial angular momentum vector of the disk is not aligned with the symmetry axis of it's repsective potential. The potentials used in the following simulations are static, and the z-axis is the symmetry axis. The template potential that has been adopted for this study has the form,

$$\Phi = \frac{v_0^2}{2} \ln\left(x'^2 + y'^2 + \frac{z'^2}{q^2}\right), \qquad (1)$$

where v_0 is a constant circular speed and the q factor determines the degree of oblateness ($q < 1$) of the halo. The potentials that will be discussed in this study have fixed $v_0 = 1$ and differ only in their q values. The primed coordinates (x', y', z') that have been introduced in eq.(1) will hereafter be referred to as the halo coordinates. The other coordinates that we will refer to are represented by unprimed variables (e.g., x, y, z). The unprimed coordinates are related to the halo coordinates through a twenty degree rotation in the counter-clockwise direction about their common x/x'-axis. Since all disks in this study are initially axisymmetric in the (x, y) plane, these coordinates are called the disk coordinates. Schematically, the situation is shown from the perspective of an observer on the x/x'-axis in Fig. 1.

3. Nonself-Gravitating Particle Ring Simulations

As a first step towards understanding the complex behavior of fully three-dimensional gas disks, we have constructed rings of nonself-gravitating point masses. We have followed the evolution of these rings in potentials like eq.(1) for four different q values, $q = 0.99, 0.95, 0.9$, and 0.8. The dynamics of these particles are followed using a Verlet finite-difference scheme for solving the equations of motion (Verlet 1967). Energy is conserved satisfactorily ($\Delta E/E \approx 10^{-5}$). The rings are composed of one hundred unit mass particles that are initially in planar circular orbits with radius $R_{\rm ring} = 1.0$ and velocity $v_{\rm circ} = 1.0$ in the (x, y) plane, where $R^2_{\rm ring} = x^2 + y^2$.

Since there is no particle self-interaction, each particle orbit freely precesses according to the quadrupole moment of the potential. After a given number of precession periods ($t \approx 1.5\, \tau_{\rm prec}$, see eq.[3]), a planar ring description of the system becomes insufficient as the particle motions lose coherence. This is evidenced by the formation of two diametrically opposed "bunches" of particles as well as a noticeable vertical position spread (see Figs. 2 & 3). After $t \approx 8\, \tau_{\rm prec}$, the ring particles phase mix. The resulting thick ring is centered vertically on the potential's equatorial plane. This behavior is a kind of dissipationless settling, conserving $J_{z'}$, the z'-component of angular momentum in the halo frame, while removing $J_{x'}$ and $J_{y'}$ from the ring. [DO WE NEED A FIGURE SHOWING THE EVOLUTION OF Jx, Jy, AND Jz?]

Since $\omega_{\rm prec} \sim 1/R$ (see eq.[3]), a "disk" of particles can be created by taking snapshots of the ring particles at different times. To illustrate the point, imagine that the outer ring of the "disk" ($R = 1.0$) is taken from the snapshot at $t = 0.1\, \tau_{\rm prec}$. The inner ring of the "disk" ($R = 0.1$) is then taken from the snapshot at $t = 1.0\, \tau_{\rm prec}$ and the middle ring ($R = 0.5$) corresponds to the ring at $t = 0.2\, \tau_{\rm prec}$. Figure 4 shows two views of such a disk. In this case, the inner ring has precessed 1.235 times. In anticipation of future figures, Fig. 5 illustrates a similar disk with the positions of a (y, z) slice through the disk marked by asterisks. In this figure, the inner ring has precessed 2.47 times.

We expect that the correspondence between the particle disks and the fluid disks will be short lived for the following reason. The particles in the disks discussed above do not interact. Fluid elements of nonself-gravitating gas disks interact through pressure. So, once the particle bunching occurs, the two systems must take divergent paths. This is neither surprising nor illuminating. However, the particle ring simulations have given us a believable benchmark to check the early evolution of our gas disks against. We now turn our attention to those fluid simulations.

4. Gas Disk Settling Simulations

4.1. Initial Models

Initial equilibrium gas disks (rotationally flattened tori) have been created using the Hachisu Self Consistent Field (HSCF) technique (see Hachisu 1986 for a full discussion of the method). The basic idea behind the HSCF is that a steady-state, equilibrium system with an axisymmetric velocity field has no variation in its "specific energy". More specifically, the combination of a system's enthalpy, gravitational potential energy, and centrifugal potential energy should have no gradient. Using a polytropic equation of state (EOS) for the fluid allows the enthalpy to be expressed in terms of the density. The gravitational potential is related to the density through Poisson's equation. By choosing a specific axisymmetric form for the centrifugal potential and enforcing the constant "specific energy" requirement, an equilibrium density distribution can be found.

In this study, the resulting density distributions are in equilibrium for a spherically symmetric ($q = 1.0$) potential with the form of eq.(1). The initial disks have centrifugal potentials determined from rotation laws of the form,

$$\Omega(R) \propto R^{-(1+\alpha)}. \qquad (2)$$

In this way, the disk is not completely supported by rotation and allows for some amount of pressure support, dependent on α.

4.2. Fluid Dynamics Code

All gas disk simulations have been performed with an Eulerian fluid dynamics code that has been described fully in Motl, Tohline, & Frank (2001). However, it is worth mentioning the five attributes of this code that are relevant to this study. One, there is no explicit inclusion of physical viscosity. Numerical viscosity, however, is always present, and its impact is discussed later. Two, self-gravity is not included in these gas disks. The only source of gravity is a potential with the form of eq.(1). Three, the code is fully three-dimensional, allowing complex, asymmetric features to evolve. Four, the fluid is evolved adiabatically (i.e. there is no entropy increase). Five, the computational grid has cylindrical symmetry.

4.3. Disk Evolutions

While the available parameter space for these simulations is large, we decided to focus on halo oblateness (q values). To this end, we fixed the following parameters for all simulations discussed below. First, the initial inclination angle of all disks is $20°$. This is the angle between the disk's angular momentum vector and the z-axis. Initially, there is no twist angle. Second, the EOS is that of an $n = 3/2$ polytrope. Third, the value of α in the rotation law (eq.[2]) is $\alpha = 0.02$. These parameters define the standard initial disks.

4.3.1. $q = 0.8$

Setting $q = 0.8$ in eq.(1) provides the most oblate potential used in this study. For clarity, we will refer to this potential as the "reference" potential. We have performed two simulations using the reference potential. The purpose of these simulations was to determine the impact of numerical viscosity. Numerical viscosity is present in any finite-difference fluid dynamics code. It is a by-product of the stabilization of the method of solving partial differential equations numerically and is dependent on grid resolution. If numerical viscosity is an important piece of the dynamics of a fluid system, then simulations with different resolutions should produce different results. Accordingly, we first evolved a disk model on a 64^3 cylindrical grid for $\approx 4\,\tau_{\rm prec,0.8}$, where $\tau_{\rm prec,0.8}$ is the precession period in the middle of the disk ($R = 0.5$) for a $q = 0.8$ potential. For logarithmic potentials, the precession frequency is given by (Steiman-Cameron & Durisen 1988),

$$\omega_{\rm prec}(R) = -\frac{3}{4}\eta \cos i_0 \frac{v_0}{R}, \qquad (3)$$

where $\eta = \frac{2-2q^2}{1+2q^2}$ and i_0 is the inclination angle of the disk and the minus sign is due to $q < 1$. Since $\omega_{\rm prec}$ is dependent on q and $\tau_{\rm prec} = 2\pi/|\omega_{\rm prec}|$, we include the q value subscript on $\tau_{\rm prec}$ values. For $q = 0.8$, the precession timescale is approximately 4.5 times longer than the orbital period at $R = 0.5$. Next, a disk model was evolved on a 128^3 cylindrical grid for $\approx 3\,\tau_{\rm prec,0.8}$. From the extremely similar appearance of the two models at comparable times in the evolutions and the similar settling times, we determined that numerical viscosity does not play a significant role in the simulations.

Focusing now on the 128^3 resolution simulation, Fig. 6 contains isodensity contour plots for (y, z) plane cross-sections of the disk at 8 different times. The time listed for each slice is in units of $\tau_{\rm prec,0.8}$. As the disk settles towards its new equilibrium, there is also a redistribution of material and angular momentum. The correspondence between the early stages of the particle ring and gas disk evolutions is shown in Fig. 7. A cross-section isodensity plot of the gas disk at $0.247\,\tau_{\rm prec,0.8}$ is shown with the equivalent particle disk superimposed. The asterisks mark the positions at which the particle rings cross the (y, z) plane.

Fig. 8 focuses on the $t = 0.890\tau_{\rm prec,0.8}$ frame of Fig. 6. From this "edge-on" view, the disk warp is evident at large radii. Also, the disk appears to have corrugations which persist even when most of the gas has settled into the halo equatorial plane, $t \approx 1.8\,\tau_{\rm prec,0.8}$ (see the last frame of Fig. 6). Fig. 9 presents views of the surface density, as seen from the z axis, showing major nonaxisymmetric structure in the disk that continues even after the disk appears to lie completely in the potential's equatorial plane. Leading spiral arms form early in the settling due to the retrograde precession of the fluid elements. As the spiral features disappear, a bar distortion is seen in the central region of the disk. Figure 10 illustrates that the settling behavior is approximately exponential in time for all radii. Further discussion of this behavior is given in §5.

4.3.2. $q = 0.9$

The disk simulation in the $q = 0.9$ potential has been carried out on a 128^3 cylindrical grid. The increase in q has also led to an increase in $\tau_{\rm prec,0.9}$. Specifically, precession time for orbits of a given radius in the $q = 0.9$ case is approximately twice as long as in the $q = 0.8$ case (i.e. $\tau_{\rm prec,0.9} \approx 9.8\,\tau_{\rm orb}$). The $q = 0.9$ simulation is very similar to the $q = 0.8$ simulation in a qualitative sense. The $q = 0.9$ disk develops corrugations, a warp, and leading spiral features. Also, when the $q = 0.9$

disk appears to be settled in the halo equatorial plane (after $\approx 1.6\tau_{\rm prec,0.9}$), there is a bar distortion present in the center. Further, the settling again appears to be approximately exponential in time (see Fig. 11)[THIS FIGURE HAS NOT BEEN MADE YET]. The differences between the $q = 0.8$ and $q = 0.9$ simulations are mostly ones of magnitude. The development of nonaxisymmetric structure is slower for the $q = 0.9$ case. Also, the bar that is present at the end of the $q = 0.9$ simulation appears weaker than the one in the $q = 0.8$ disk.

4.3.3. $q = 0.95$

As before, the $q = 0.95$ simulation utilized a 128^3 cylindrical grid. The precession time is approximately twenty times as long as the orbital period. As in the previous two cases, this disk also develops corrugations, a warp, and leading spiral features. However, the spiral features are noticeably weaker in this case. Also, while the central region of the settled $q = 0.95$ disk is asymmetric, it is no longer obvious that there is a simple bar distortion. Overall, the settling process in this case seemed more gentle than the previous two simulations, taking $\approx 32\tau_{\rm orb}$ to reach the halo equatorial plane. This relative gentleness is to be expected in a more spherical potential. However, unlike the previous two cases, the settling behavior can not be approximated with an exponential time dependence (see Fig. 12) [THIS FIGURE HAS NOT BEEN MADE YET].

5. Analysis of Gas Disk Simulations

In an effort to describe the gas disk simulations more quantitatively, we have analyzed the energy and angular momentum conservation as well as the inertia tensor of the disks. The energy and components of the inertia tensor are defined in the disk coordinate system since the quantities of interest are specified in this system. We calculate cartesian components of the inertia tensor (e.g., $I_{\rm xy}$) for cylindrical shells of material due to the geometry of the system. As a check of our calculations, we have also calculated inertial tensors for spherical shells, and the results are similar. Once the inertia tensor is diagonalized, the relative magnitudes of the principal moments of inertia and their associated eigenvectors give us information about the angular momenta of the material in the shells.

5.1. Energy Conservation

Figure 13 illustrates the conservation of energy of the disk in the $q = 0.8$ potential as well as the behavior of various energies relevant to the disk. The gravitational potential energy W is not shown because a nonself-gravitating system in the logarithmic potential of eq.(1) has $W = -M_{\rm tot}$, where $M_{\rm tot}$ is the mass of the system, which is constant. Recall that these energies are defined with respect to the disk coordinate system. As such, there is no radial/vertical kinetic energy $T_{\rm rz}$ for the initial model. As the disk settles towards the halo equatorial plane, $T_{\rm rz}$ increases rapidly at first and then quickly settles to a lower, but nonzero, value. In almost mirror-image fashion, the kinetic rotational energy $T_{\rm rot}$ drops in the early stages of the settling and then rises towards a fairly constant value. The thermal energy $T_{\rm therm}$ rises an extremely small amount during the settling, indicating that random motions (and hence the pressure) never dominate the dynamics. By the end of the simulation ($t = 3.1\ \tau_{\rm prec,0.8}$), the system appears to be in energy equilibrium.

5.2. Disk Tilting & Twisting

By monitoring the direction of the angular momentum vector of each annulus of material throughout the simulation, we can analyze the settling with two angles. One of these is what we call the tilt β. β is the angle between the z-axis and an angular momentum vector. The other angle will be called the twist $\gamma(R)$. The twist is the angle between the projection of the angular momentum vector onto the halo equatorial plane and the line of nodes of the disk. Initially, $\beta = 20°$ and $\gamma(R)$ is undefined. As the settling proceeds, we expect β to decrease to $0°$. At the same time, $\gamma(R)$ should be increasing with time as the line of nodes differentially precesses.

When we look at the behavior of the tilt and twist angles for these simulations, the following behavior appears. The tilt angle does indeed decrease towards $0°$, and, to zeroth order, the settling rate is constant over the entire disk. This is most evident when β vs. R is plotted for several different times in the $q = 0.8$ case (Fig. 14) [THIS MIGHT LOOK BETTER AS A MOVIE

ALSO]. Referring back to Fig.10, we can see that the settling at four different radii proceed in approximately the same manner. Additionally, figures 10 & 11 show that the settling is approximately exponential for the $q = 0.8$ and $q = 0.9$ cases. This is interesting because some viscous disk settling models also predict exponential settling in time (Steiman-Cameron & Durisen 1988, 1990; New *et al.* 1998). So, despite a significant change in evolution (viscous vs. nonviscous), our simulations qualitatively resemble previous models.

As expected, the twist angle increases steadily early in the settling process. However, there is a point in each of the simulations at which the twisting stops. This behavior is shown for the reference case in Fig. 15. Along with the solid curves that represent the measured twist angle, the dash-dot curve shows the analytical prediction for stress-free precession, i.e., precession with no viscosity. This curve describes how the particle ring constituents precess, for example. The curves increase downward due to the retrograde nature of the precession. A critical pitch angle γ_c of the twist pattern can be determined for the gas disks once the twisting stops. γ_c increases with increasing q values: for $q = 0.8$, $\gamma_c = 16°$; for $q = 0.9$, $\gamma_c = 18°$; for $q = 0.95$, $\gamma_c = 30°$. [DO WE WANT TO INCLUDE THE MATHEMATICAL DISCUSSION OF THE SHOCKS HERE?]

5.3. Disk Moments of Inertia

[DOES THIS SECTION NEED FIGURES OR A LINK TO THE MOVIES OF THE EVOLUTION OF THE MOMENTS OF INERTIA?] We can use the measured principal moments of inertia to investigate the symmetry of the disk during its settling. Since the disk stays thin, the maximum moment of inertia corresponds to the direction normal to the disk. Initially, the remaining two moments are equal because of the axisymmetry of the initial state. As the settling progresses, however, the ratio of the nonmaximum moments differs from unity, indicating nonaxisymmetry. It is interesting to note that even after the disk appears to have settled in the halo equatorial plane, this ratio is still different from one. Looking at the surface densities of disks that have settled to the halo equatorial planes also reveals the asymmetries (see, for example, Fig. 9). The central regions of the disks in all three simulations appear to be dominated by an $m = 2$ distortion. Also, the contours in the outer regions of the disks appear to have slightly elliptical shapes.

6. Conclusions

In an effort to understand the formation and maintenance of warped galactic HI disks, we have performed simulations of nonequilibrium nonviscous gas disks in static halo potentials. Specifically, the angular momentum vectors of the disks have been tilted with repect to the axis of symmetry of the halo potential. This tilt introduces torques on the disk and drives it towards the equatorial plane of the halo potential. Intermediate stages of this settling process have the general appearance of observed warped HI disks.

Two of the disks appear to settle exponentially with time, while the third (evolved in the most spherical halo potential investigated) has a more complex settling behavior. This is similar to the previously determined settling behavior of viscous disks. The puzzling feature of this similarity is that our disks have no explicit viscosity. One possible way to explain this is that small shocks provide an effective viscosity. The evidence for these shocks may be the existence of the critical pitch angle of the twist pattern. The gas disks are differentially twisted to a point at which noncircular streamlines are brought into contact and a shock forms. Thus, the twisting stops at γ_c and there is a resistance to continued twisting.

We conclude that if warped HI disks are due to a misalignment of the angular momentum of the disk and the symmetry axis of the halo potential, then observed warps can be explained in two ways. One, galactic halo potentials are significantly flattened making the settling process fairly rapid and warps short-lived features. Two, galactic halo potentials are nearly spherical and the settling process is fairly slow. In this case, the observed warps can be long lived patterns. Despite this degeneracy, such disks will settle in a coherent fashion and will halt their differential twisting at some critical pitch angle. These disks will also be significantly nonaxisymmetric, even after settling to the halo equatorial plane.

REFERENCES

Battaner, E., Florido, E., & Sanchez-Saavedra, M.L. 1990, A&A, 236, 1

Binney, J. 1978, MNRAS, 183, 779

Binney, J. 1981, MNRAS, 196, 455

Bosma, A. 1981, AJ, 86, 1791

Briggs, F.H. 1990, ApJ, 352, 15

Chaves, T.A., & Irwin, J.A. 2001, ApJ, 557, 646

Fletcher, A., & Shukurov, A. 2001, MNRAS, 325, 312

Giovanelli, R., & Haynes, M.P. 1988, in Galactic and Extragalactic Radio Astronomy, ed. Verschuur, G.C. and Kellerman, K.I., (New York:Springer-Verlag)

Gordon, K.J. 1971, ApJ, 169, 235

Hachisu, I. 1986, ApJS, 61, 479

Hofner, P., & Sparke, L.S. 1994, ApJ, 428, 466

Hunter, C., & Toomre, A. 1969, ApJ, 155, 747

Kahn, F.D., Woltjer, L. 1959, ApJ, 130, 705

Lewis, B.M. 1968, Proc. Astron. Soc. Australia, 1, 104

López-Corredoira, M., Betancort-Rijo, J., & Beckman, J.E. 2002, astro-ph/0202156

Lynden-Bell, D. 1965, MNRAS, 129, 299

Motl, P.M., Tohline, J.E., Frank, J. 2001, ApJ, submitted

New, K.C.B., Tohline, J.E., Frank, J., & Väth, H.M. 1998, ApJ, 503, 632

Rogstad, D.H., Lockhart, I.A., & Wright, M.C.H. 1974, ApJ, 114, 385

Sancisi, R. 1976, A&A, 53, 159

Sparke, L.S. 1986, MNRAS, 219, 657

Sparke, L.S., & Casertano, S. 1988, MNRAS, 234, 873

Steiman-Cameron, T.Y., Durisen, R.H. 1988, ApJ, 325, 26

Steiman-Cameron, T.Y., Durisen, R.H. 1990, ApJ, 357, 62

Tohline, J.E., Simonson, G.F., & Caldwell, N. 1982, ApJ, 252, 92

Tubbs, A.D., & Sanders R.H. 1979, ApJ, 230, 736

Tubbs, A.D. 1980, ApJ, 241, 969

van den Bosch, F.C., Abel, T., Croft, R.A.C., Hernquist, L., & White, S.D.M. 2002, astro-ph/0201095

Verlet, L. 1967, Phys. Rev., 159, 98

Wright, M.C.H., Warner, P.J., Baldwin, J.E. 1972, MNRAS, 155, 337

This 2-column preprint was prepared with the AAS LaTeX macros v5.0.

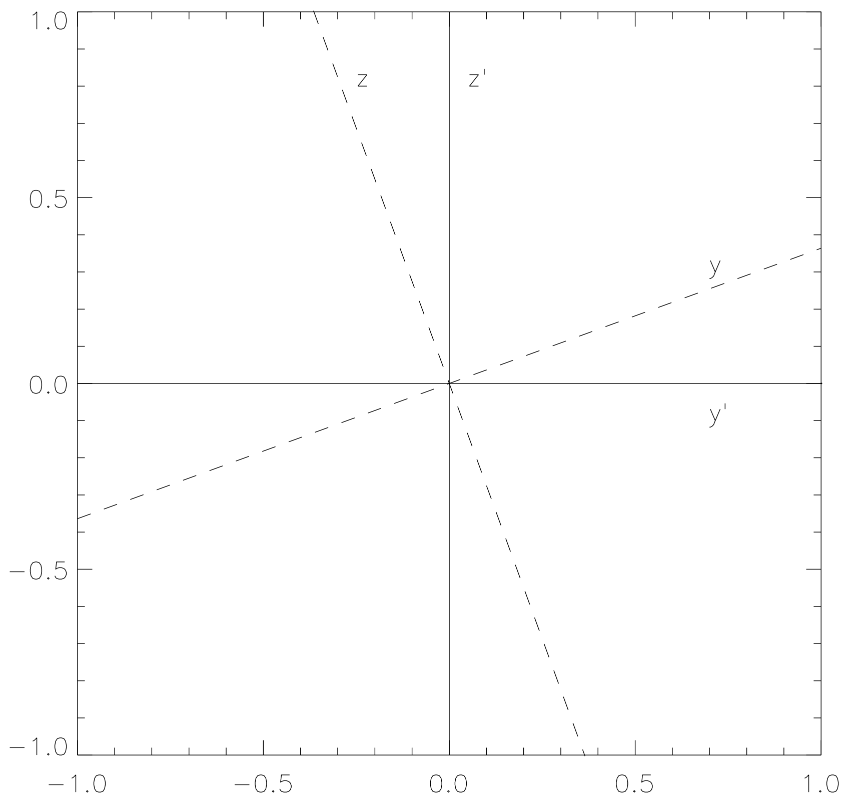

Fig. 1.— Plot of the relation between the halo (y', z') coordinates and the disk (y, z) coordinates as seen from their common x-axis.

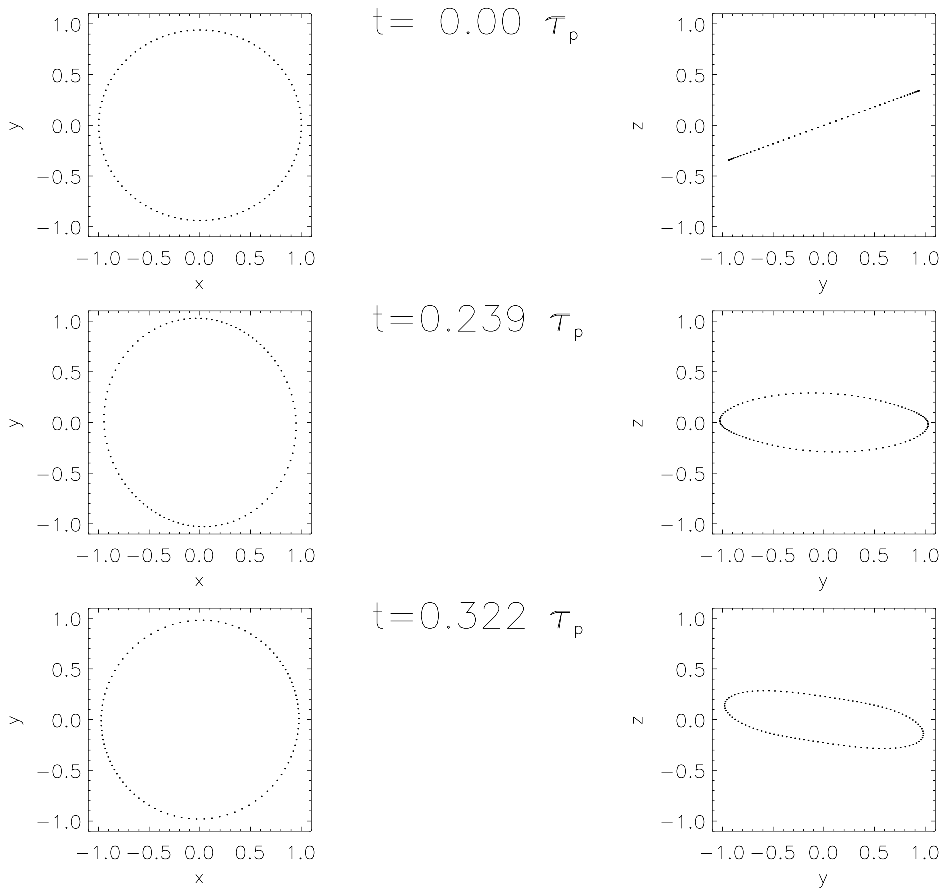

Fig. 2.— Sequence of plots detailing the time evolution of a single nonself-gravitating particle ring as seen in the halo coordinate system. The evolution takes place in the reference potential.

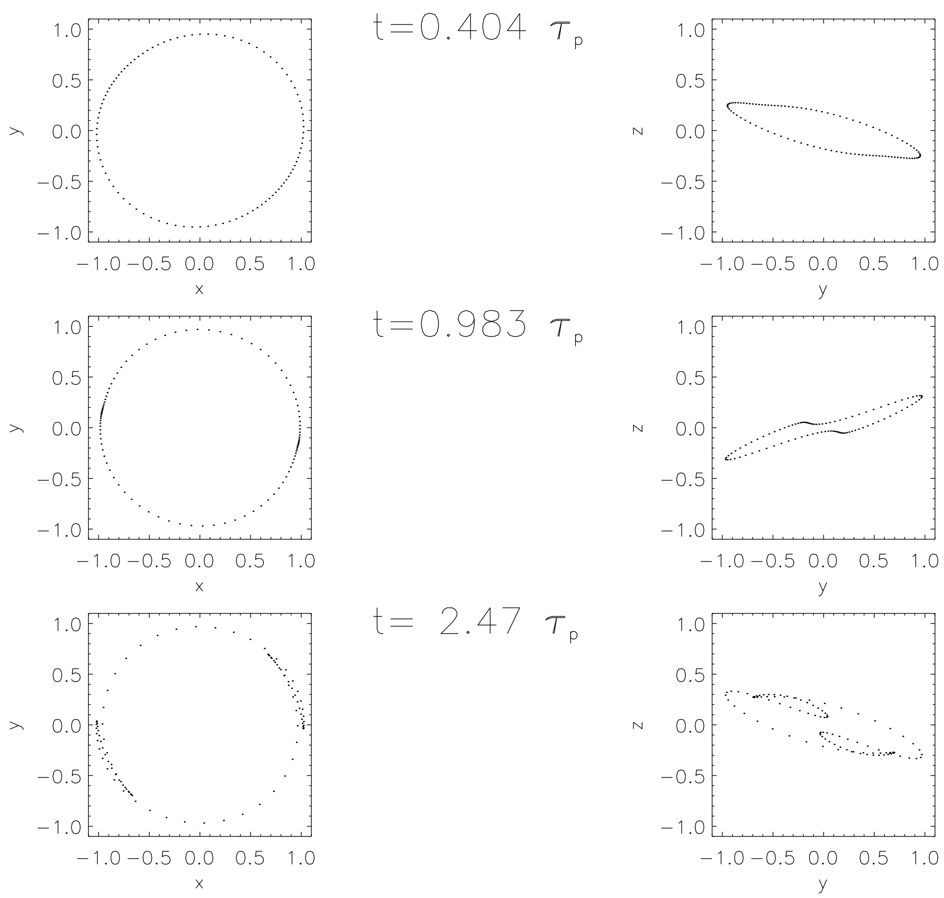

Fig. 3.— Continuation of plots detailing the time evolution of a single nonself-gravitating particle ring as seen in the halo coordinate system.

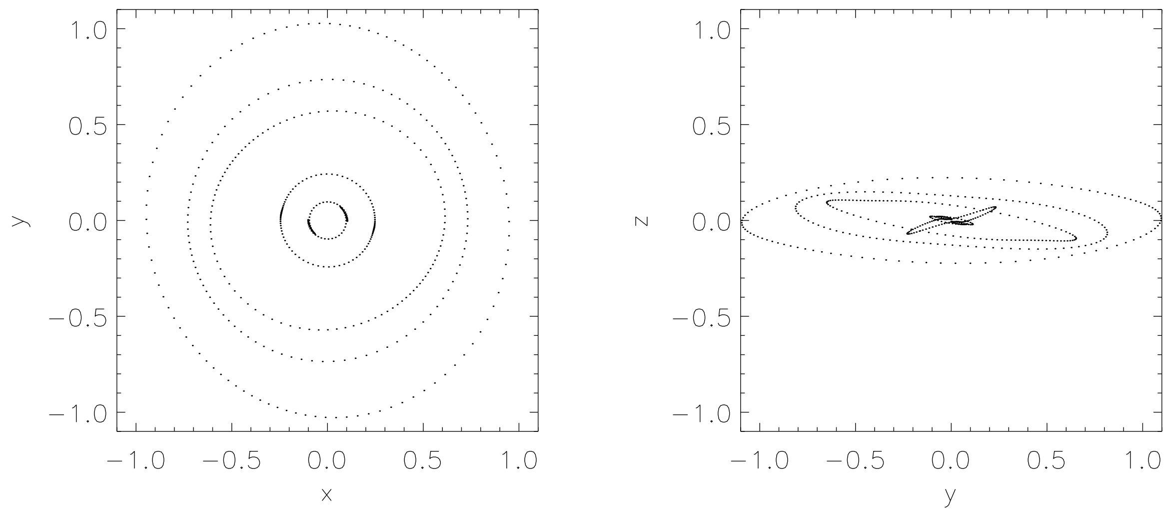

Fig. 4.— Frames showing two halo coordinate system views of a “disk” composed of rings of particles after the inner ring has precessed 1.235 times. Each ring has been evolved in the reference potential.

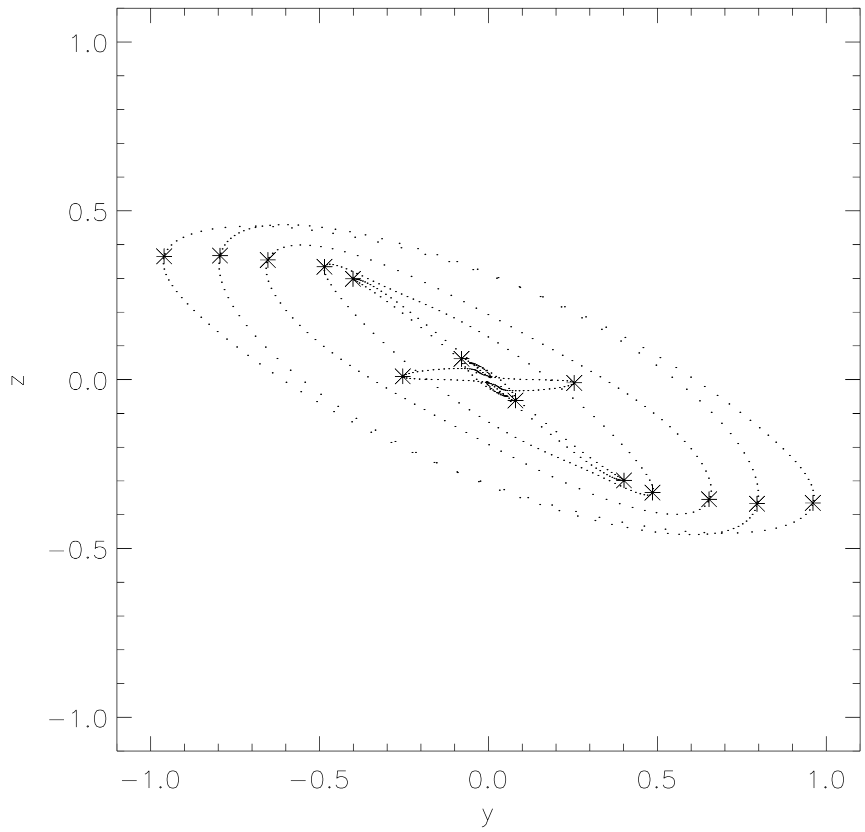

Fig. 5.— Plot showing a particle ring disk after the inner ring has precessed 2.47 times. The asterisks mark the positions at which each ring intersects the (y, z) plane. Again, the rings have been evolved in the reference potential.

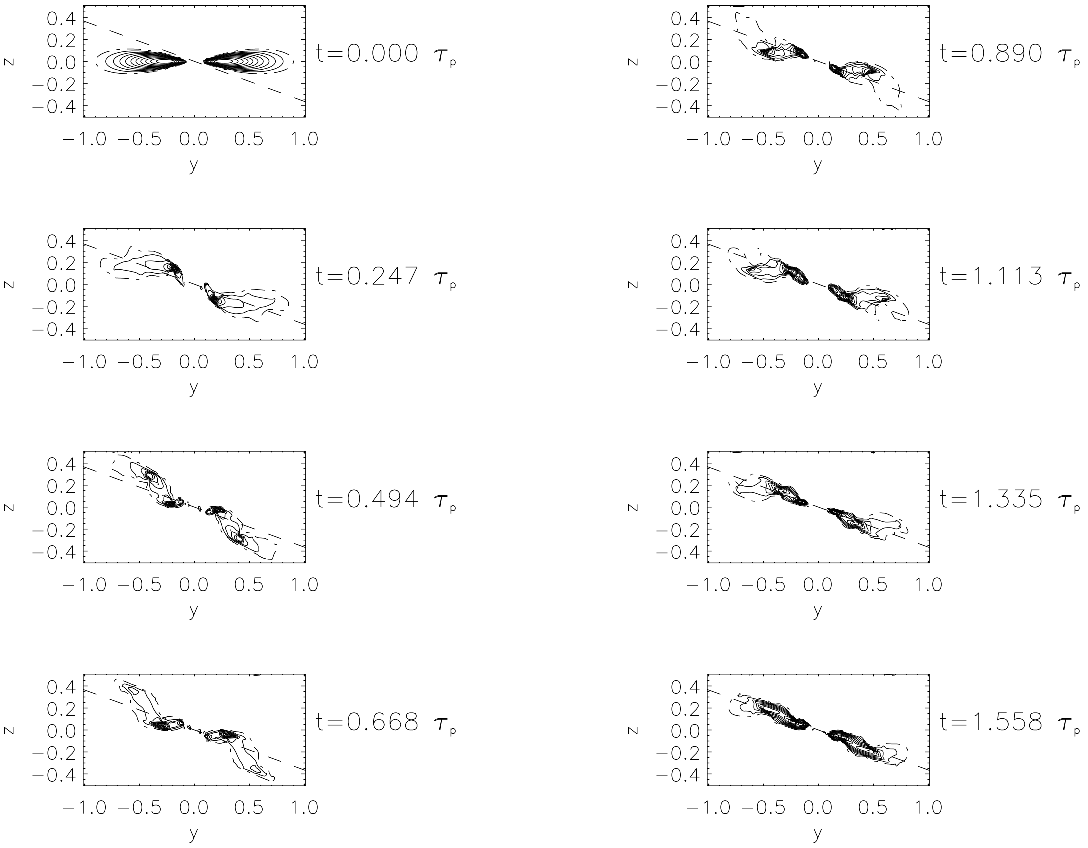

Fig. 6.— Sequence of plots showing (y, z) plane cross-section isodensity contours. The tilted dashed lines mark the locations of the potential's equatorial (x', y') plane. Note the corrugations that still exist in the disk even after it has settled to the (x', y') plane.

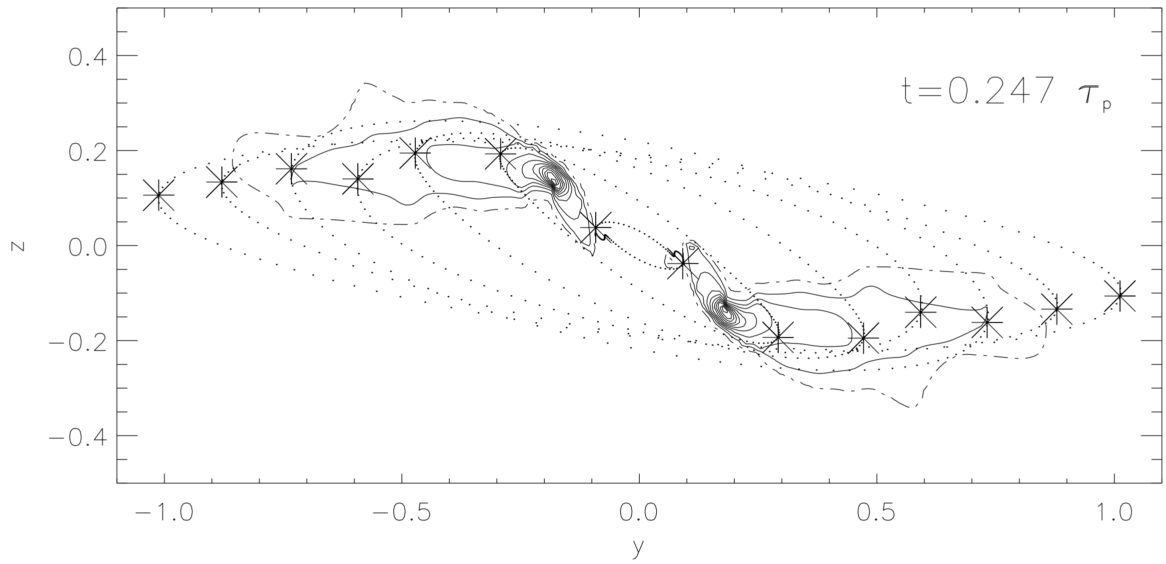

Fig. 7.— Plot showing the correspondence between the early stages of the gas disk and particle disk simulations. The asterisks mark the positions at which the particle disk crosses the (y, z) plane. Both disks have been evolved for $0.247\,\tau_{\rm prec,0.8}$ at $R = 0.5$.

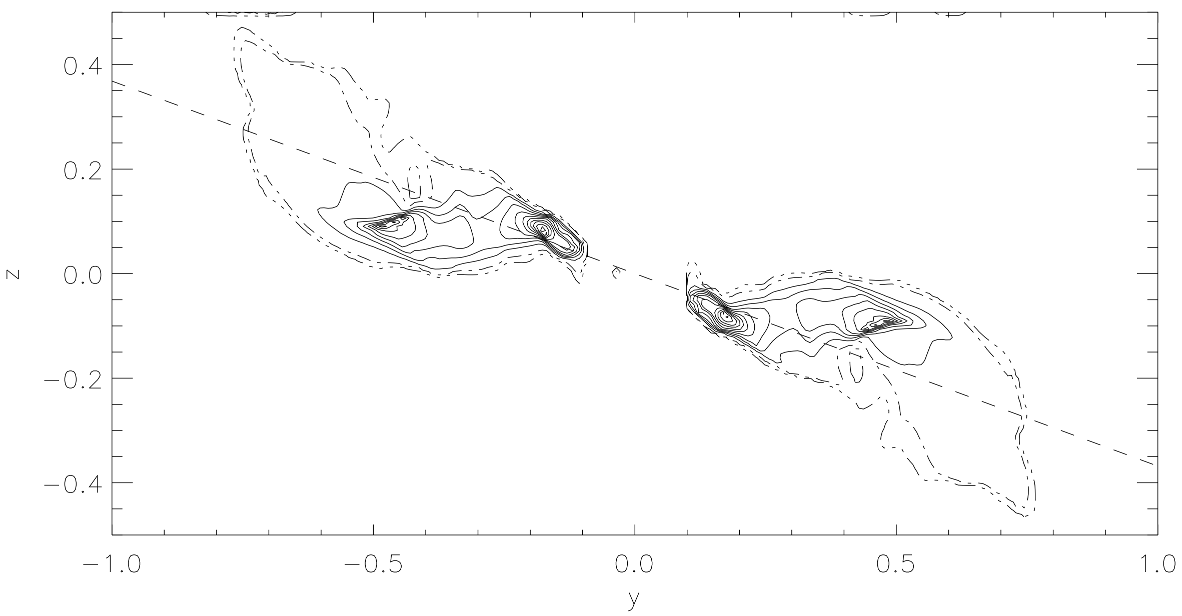

Fig. 8.— Detailed view of the $t = 0.890\tau_{\rm prec}$ frame from Fig. 6. Note the prominent warp in the outer regions of the disk as well as the corrugations that are also present.

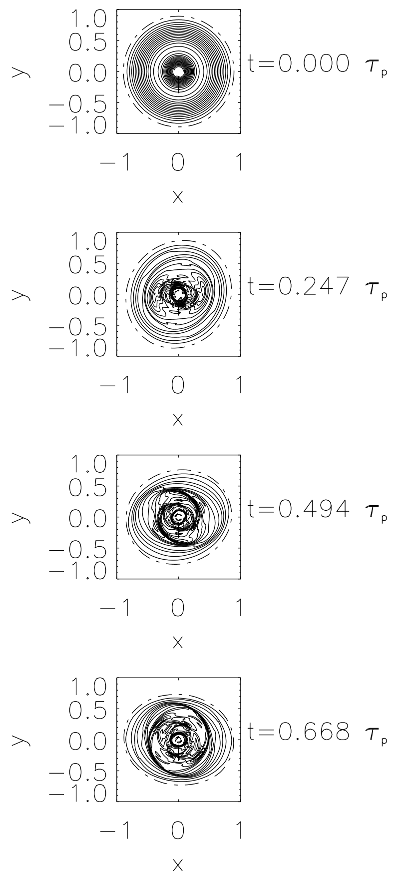

Fig. 9.— Sequence of plots showing surface density contours along the z' axis. These frames are the top-down views of the same disks shown in Figure 6.

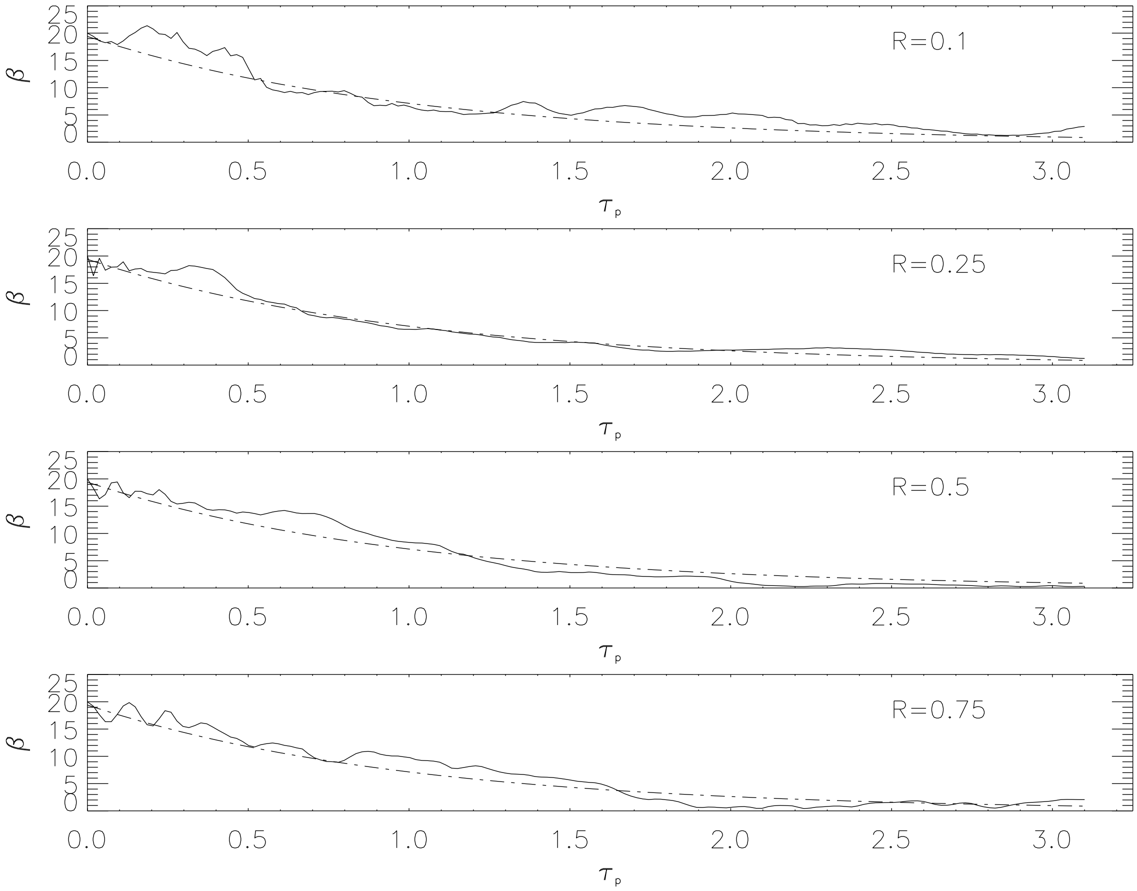

Fig. 10.— Plot of the settling behavior versus time at four different radii for the $q = 0.8$ simulation. The angle β is given in degrees and measures the tilt angle of the disk. The settling appears to be approximately exponential at all radii.

Fig. 11.— Plot of the settling behavior at four different radii for the $q = 0.9$ simulation. As in the $q = 0.8$ case, the settling appears to be approximately exponential at all radii.

Fig. 12.— Plot of the settling behavior at four different radii for the $q = 0.95$ simulation. Unlike the $q = 0.8$ and $q = 0.9$ cases, the settling behavior of this disk does not appear exponential at any radius.

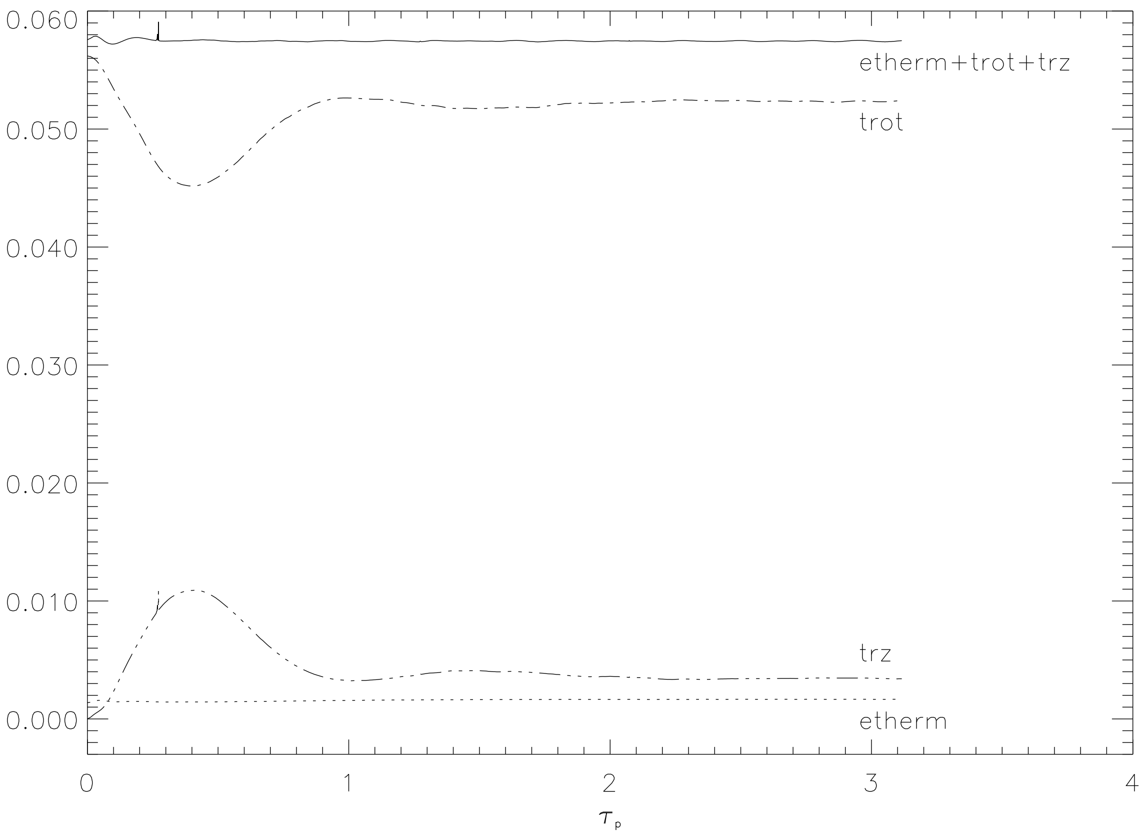

Fig. 13.— Plot illustrating the behavior of various energies in time. The energies are measured in the disk coordinate system. The solid line is the total energy. The kinetic energy of rotation is marked with the dashed line. The dot-dash line denotes the kinetic energy associated with radial and vertical motion. The gravitational potential energy is not shown since it is constant in time for nonself-gravitating systems in logarithmic potentials.

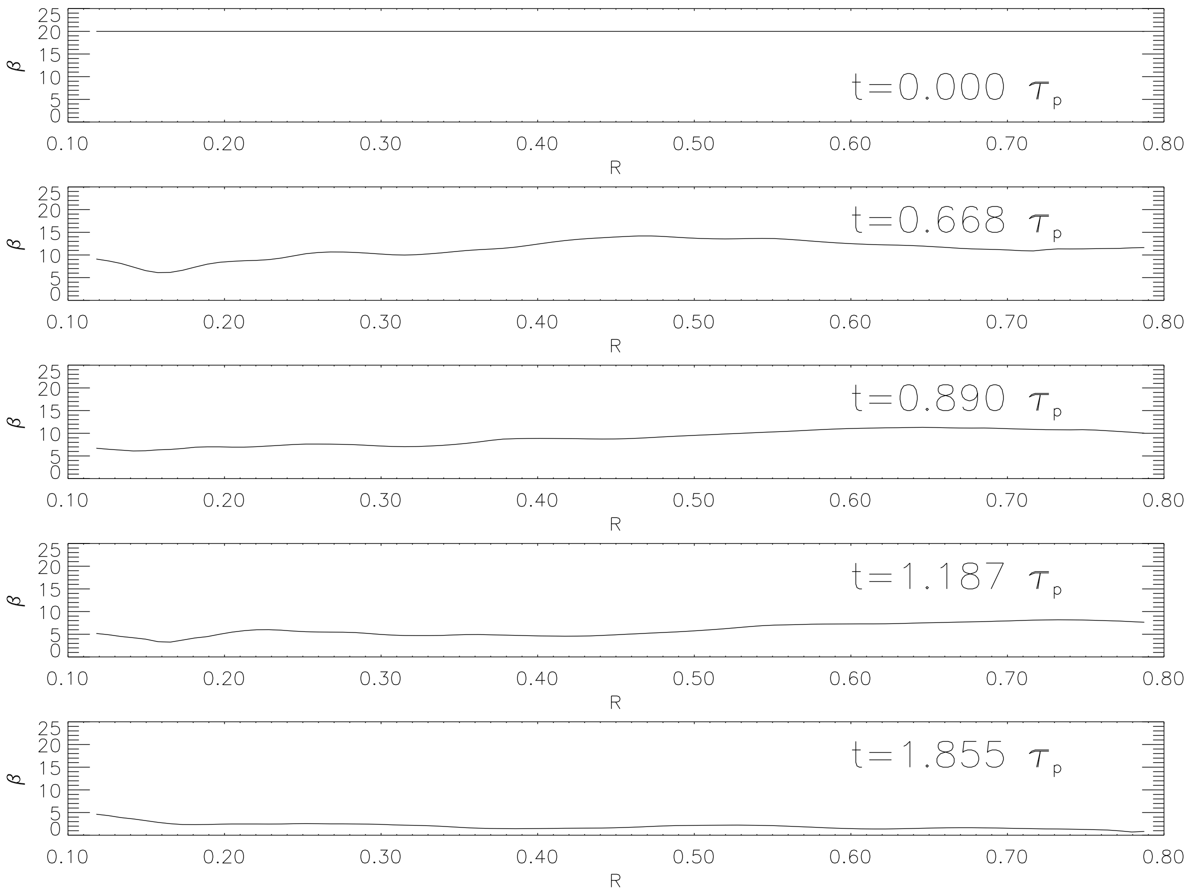

Fig. 14.— Sequence of plots illustrating the settling behavior versus radius at several times in the evolution of the disk in the reference potential. This may be replaced by a movie showing the settling behavior.

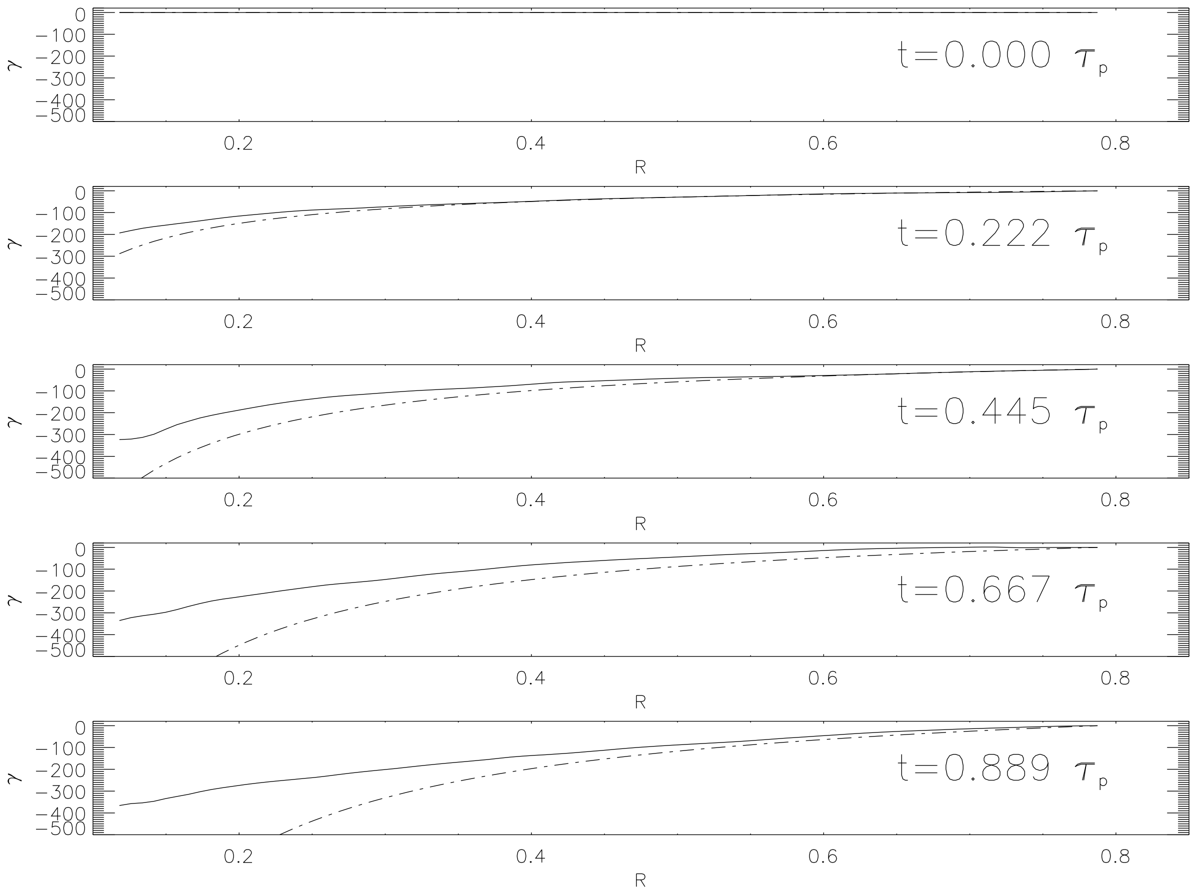

Fig. 15.— Sequence of plots showing the behavior of the twist angle γ behavior versus radius at several different times. The γ values have been normalized so that the outermost value remains constant. The downward pointing shape of the curve is due to the retrograde nature of the precession. The dash-dot curve is the anlytical prediction for stress-free precession.